Journal of Computational Physics 231 (2012) 6181–6191

Contents lists available at SciVerse ScienceDirect

Journal of Computational Physics

journal homepage: www.elsevier.com/locate/jcp

Boundary element dynamical energy analysis: A versatile method for solving two or three dimensional wave problems in the high frequency limit

David J. Chappell *, Gregor Tanner, Stefano Giani

School of Mathematical Sciences, University of Nottingham, University Park, Nottingham NG7 2RD, UK

ARTICLE INFO

Article history:
Received 31 August 2011
Received in revised form 17 May 2012
Accepted 18 May 2012
Available online 31 May 2012

Keywords:
Statistical energy analysis
High-frequency asymptotics
Perron–Frobenius operator
Boundary element method

ABSTRACT

Dynamical energy analysis was recently introduced as a new method for determining the distribution of mechanical and acoustic wave energy in complex built up structures. The technique interpolates between standard statistical energy analysis and full ray tracing, containing both of these methods as limiting cases. As such the applicability of the method is wide ranging and additionally includes the numerical modelling of problems in optics and more generally of linear wave problems in electromagnetics. In this work we consider a new approach to the method with enhanced versatility, enabling three-dimensional problems to be handled in a straightforward manner. The main challenge is the high dimensionality of the problem: we determine the wave energy density both as a function of the spatial coordinate and momentum (or direction) space. The momentum variables are expressed in separable (polar) coordinates facilitating the use of products of univariate basis expansions. However this is not the case for the spatial argument and so we propose to make use of automated mesh generating routines to both localise the approximation, allowing quadrature costs to be kept moderate, and give versatility in the code for different geometric configurations.

1. Introduction

Predicting the wave energy distribution of the vibro-acoustic response of a complex mechanical system is a challenging task, especially in the mid-to-high frequency regime. Standard numerical tools such as finite element methods become inefficient, and ray or thermodynamic approaches are often employed to model the wave energy flow through the structure. Popular methods are *statistical energy analysis* (SEA) [1–3], in which the mean energy flow between subsystems is assumed to be proportional to the energy gradient, and the *ray tracing technique*, in which the wave intensity distribution is determined by summing over contributions of a potentially large number of ray paths [4–6].

SEA is in fact a low resolution ray tracing method [7,8] leading to small numerical models compared to ray tracing. This efficiency saving comes at a price, however: SEA has no spatial resolution of the energy distribution within subsystems and becomes unreliable whenever long range correlations in the ray dynamics are present. The recently developed *dynamical energy analysis* (DEA) [8,9] provides a tool which interpolates between SEA and a full ray tracing analysis and can overcome some of the problems mentioned above at a relatively small computational overhead. DEA thus enhances the range of applicability of standard SEA and gives bounds on the range of applicability of SEA. Related methods have been discussed

* Corresponding author.
E-mail addresses: david.chappell@nottingham.ac.uk (D.J. Chappell), gregor.tanner@nottingham.ac.uk (G. Tanner), stefano.giani@nottingham.ac.uk (S. Giani).

0021-9991
http://dx.doi.org/10.1016/j.jcp.2012.05.028

previously in the context of wave chaos [10] and structural dynamics [11]. In particular Langley's *wave intensity analysis* (WIA) [12,13] and Le Bot's thermodynamical high frequency boundary element method [14–16] include details of the underlying ray dynamics. The approach employed here differs from these methods by considering multiple reflections in terms of linear operators. Representing these operators in terms of basis function expansions then leads to SEA-type equations.

In this work we develop a new approach to DEA suitable for modelling three-dimensional problems. The present DEA methods rely on the fact that one can easily parametrise the boundary of the region being modelled, and then apply an orthonormal basis approximation over the resulting boundary phase space coordinate system. In two dimensions this is simple as the boundary may be parametrised along its arc-length and the associated momentum (or direction) coordinate taken tangential to the boundary. The basis can be any suitable (scaled) univariate basis in both position and momentum, such as a Fourier basis [8] or Chebyshev polynomials [9]. Defining a suitable parametrisation for the spatial coordinate in three-dimensions becomes much more difficult. In momentum space spherical polar coordinates may be employed and so these problems do not arise.

In order to develop a flexible code we employ automated mesh generating routines to provide a widely applicable parametrisation of the boundary surface for general three-dimensional structures via triangulation. The precision of the spatial approximation may then be improved by refining the mesh, avoiding the issue of finding a suitable basis. One avenue for potential future study stems from the fact that it is possible to define an orthogonal basis on a general triangle which reduces to Legendre polynomials along one edge of the domain triangle [17]. However, in this work we restrict to a piecewise constant approximation on each element of the mesh for reasons of both simplicity and to keep the associated quadrature costs moderate for the three dimensional case.

For the choice of momentum basis we may take a product univariate basis as mentioned above. It is preferable if this basis is orthogonal with respect to the standard L^2 inner product for consistency with both the piecewise constant spatial approximation, and the SEA limit when the lowest order momentum basis is applied and continuity is enforced across the mesh. The main choices are either a Fourier basis or Legendre polynomials. In this work we choose Legendre polynomials due to better convergence properties in the absence of periodic boundary conditions [18] and for consistency with the approach in [17] should we wish to include a spatial basis in future work.

The remainder of the paper is structured as follows. In Section 2, the ray tracing approximation is discussed and related to the Green function using short wavelength asymptotics. In Section 3, the concept of phase-space operators is introduced in order to represent the propagation of ray densities in terms of boundary integrals. The discretization of the method using spatial meshing procedures and basis function approximations in direction space is then detailed. Decomposition of the method for problems with multiple subsystems is then discussed along with links between the method and SEA. In Section 4 the application of boundary element DEA to two-dimensional examples is discussed and verified against previous work. Finally some three-dimensional examples are considered.

2. Wave equations and asymptotics

It is assumed that the system as a whole is characterized by a linear wave equation describing the overall wave dynamics including damping and radiation in a finite domain $\Omega \subset \mathbb{R}^d,\ d = 2$ or 3. In this work only stationary problems with continuous, monochromatic energy sources are considered. We split the system into N_Ω subsystems and consider the scalar wave equation for acoustic pressure waves in each homogeneous sub-domain Ω_i, with local wave velocity $c_i, i = 1,\ldots,N_\Omega$ and $\Omega = \bigcup_{i=1}^{N_\Omega}\Omega_i$. Extensions to more complicated systems with different wave operators in different parts of the system can be treated with the same techniques as long as the underlying wave equations are linear, see the discussion in Ref. [8].

The general problem of determining the response of a system to external forcing with angular frequency ω at a source point $r_0 \in \Omega_0$ can then be reduced to solving

$$(k_i^2 - \hat{H})G(r, r_0; \omega) = -F_0\delta(r - r_0), \quad i = 1,\ldots,N_\Omega, \tag{1}$$

with $\hat{H} = -\Delta$. The Green function G represents an acoustic pressure wave where F_0 is a unit amplitude forcing term with units $kg\ s^{-2}$. The solution point is denoted $r \in \Omega_i$ and δ is the Dirac delta distribution. Furthermore, $k_i = \omega/c_i + i\mu_i/2$ is a complex valued wavenumber, where the imaginary part represents a subsystem dependent damping coefficient μ_i. Throughout this work we take $i = \sqrt{-1}$ unless used as a subscript, in which case it is an index over the number of subsystems. The wave energy density induced by the source is then given as

$$\varepsilon(r, r_0; \omega) = \frac{|G(r, r_0; \omega)|^2}{\varrho_i c_i^2}, \tag{2}$$

for $r \in \Omega_i$ where ϱ_i is the density of the medium in Ω_i. The linear wave operator $\hat{H}$ can naturally be associated with the underlying ray dynamics via the Eikonal approximation; for a more detailed derivation, see Ref. [8,19,20]. Using small wavelength asymptotics, the Green function in Eq. (1) may be written as a sum over *all* classical rays from r_0 to r for fixed kinetic energy of the hypothetical ray particle. One obtains [20,21]

$$G(r, r_0; \omega) \approx \frac{\pi}{(2\pi i)^{(d+1)/2}} \sum_{j: r_0 \to r} A_j e^{i(k_i L_j - i\nu_j \pi/2)}, \tag{3}$$

where L_j is the length of the ray trajectory between r_0 and r including possible reflections on boundaries. The amplitudes A_j may be written as a product of three terms as in Ref. [8] due to damping, mode conversion and reflection/transmission coefficients, and geometrical factors. The phase index v_j contains contributions from the reflection/transmission coefficients at interfaces between subsystems and from caustics along the ray path. Eq. (3) captures the interference patterns due to wave propagation along different 'ray' paths, but does not incorporate diffractive effects and fails at focal points (or caustics of ray manifolds in phase space) [21].[1]

Analogous representations to (3) have been considered in detail in quantum mechanics [21] and are also valid for general wave equations in elasticity, see Ref. [10] for an overview. In the latter case G becomes matrix valued. Note that the summation in Eq. (3) is typically over infinitely many terms, where the number of contributing rays increases (in general) exponentially with the length of the trajectories included. This gives rise to convergence issues, especially in the case of low or no damping [10].

The wave energy density (2) can now be expressed as a double sum over classical trajectories and hence

$$\varepsilon(r, r_0; \omega) \approx C \sum_{j,j':r_0 \to r} A_j A_{j'} e^{ik_i[L_j - L_{j'}] - i[v_j - v_{j'}]\pi/2} = C[\rho(r, r_0; \omega) + \text{off} - \text{diagonal terms}], \tag{4}$$

with $C = \pi^2 / \left(\varrho_i c_i^2 (2\pi)^{(d+1)}\right)$. The dominant contributions to the double sum arise from terms in which the phases cancel exactly; one thus splits the calculation into a diagonal part

$$\rho(r, r_0; \omega) = \sum_{j:r_0 \to r} |A_j|^2, \tag{5}$$

where $j = j'$, and an off-diagonal part. The diagonal contribution gives a smooth background signal and the off-diagonal terms describe interference effects leading to fluctuations on the scale of the wavelength. The phases related to different trajectories are (largely) uncorrelated and the resulting net contributions to the off-diagonal part are in general small compared to the smooth part, especially when averaging over frequency intervals of a few wavenumbers.

It has been shown in Ref. [8] that calculating the smooth diagonal part (5) is equivalent to a ray tracing treatment. That is, the smooth part of the energy density can be described in terms of the flow of fictitious non-interacting particles emerging from the source point r_0 uniformly in all directions and propagating along ray trajectories. This makes it possible to relate wave energy transport with classical flow equations and thus thermodynamical concepts, which are at the heart of an SEA treatment. In DEA the classical flow is expressed in terms of linear *phase space operators* as detailed in the next section.

3. Boundary integral formulation

3.1. Phase space boundary integral formulation

Following a purely kinetic viewpoint based on the interpretation that rays are trajectories of particles following Hamiltonian dynamics as detailed in Section 2 of Ref. [19], the time dependence of a density of ray trajectories (or particles) $\tilde{\rho}$ is known to satisfy the Liouville equation

$$\frac{\partial \tilde{\rho}}{\partial \tau}(X, \tau) + \frac{dX}{d\tau} \cdot \nabla_X(\tilde{\rho}(X, \tau)) = 0, \tag{6}$$

where $X = (r, p)$ denotes the phase space coordinate with position r and momentum p. The propagator for the Liouville equation is given by $K^\tau(X, Y) = \delta(X - \varphi^\tau(Y))$ and is the kernel of a linear phase space operator known as a Perron-Frobenius operator in dynamical systems theory [20,23]. The phase space flow $\varphi^\tau(Y)$ gives the position of the particle after time τ starting at $Y = (r', p')$ when $\tau = 0$. Hence we may write

$$\tilde{\rho}(X, \tau) = \int_{\mathbb{P}} K^\tau(X, Y) \tilde{\rho}_0(Y) dY, \tag{7}$$

where $\tilde{\rho}_0$ denotes the initial ray density at time $\tau = 0$. The domain of integration is over the whole of phase space $\mathbb{P} = \Omega \times \mathbb{R}^d$, where the integration over $\mathbb{R}^d$ takes care of the momentum coordinates p. Note that the flow satisfies the Hamilton equations of motion given by the system of ordinary differential equations (ODEs)

$$\frac{dX}{d\tau} = \begin{pmatrix} 0 & 1 \\ -1 & 0 \end{pmatrix} \nabla_X H, \tag{8}$$

where $H = |p|^2$ is the Hamilton function for the wave operator $\hat{H}$ in (1). That is to say, substituting $\varphi^\tau(Y)$ for $X(\tau)$ in (8) satisfies the system of ODEs with $X(0) = Y$.

[1] The short wavelength approximation can, however, be continued through focal points, giving a contribution to the phase factor v_j; an improved approximation near focal points in possible, but in general not necessary [22].

Consider a source localized at a point r_0 emitting waves continuously at a fixed angular frequency ω. Standard ray tracing techniques estimate the wave energy at a receiver point r by determining the density of rays starting at r_0 and reaching r after some unspecified time. This may be written in the form

$$\rho(r, r_0, \omega) = \int_0^\infty \int_{\mathbb{R}^d} \int_{\mathbb{P}} w(Y,\tau) K^\tau(X,Y) \rho_0(Y,\omega) dY\ dp\ d\tau, \tag{9}$$

with initial density $\rho_0(Y,\omega) = \delta(r' - r_0)\delta(k_0^2 - H(Y))$, where k_0 is the wave number at the source point as defined in Eq. (1). It can be shown that Eq. (9) is equivalent to the diagonal approximation (5) [8]. A weight function w is included to incorporate damping and reflection/transmission coefficients. It is assumed that w is multiplicative, that is, $(w(\varphi^{\tau_1}(X), \tau_2) w(X, \tau_1) = w(X, \tau_1 + \tau_2))$, which holds for standard absorbtion mechanism and reflection processes [20].

In order to solve the stationary flow problem we may rewrite Eq. (9) in boundary integral form using a boundary mapping technique. For the time being let us consider a problem with a single (sub-) system $\Omega = \Omega_1$ with boundary Γ. The Hamilton function $H = |p|^2$ is constant in this (sub-) system, that is, $|p|$ is constant. The boundary mapping procedure involves first mapping the ray density emanating continuously from the source onto the boundary Γ. The resulting boundary layer density $\rho_\Gamma^{(0)}$ is equivalent to a source density on the boundary producing the same ray field in the interior as the original source field after one reflection. Secondly, densities on the boundary are mapped back onto the boundary by a boundary integral operator $\mathcal{B}$ defined by

$$\mathcal{B}u(X^s) := \int_{\partial\mathbb{P}} K_\Gamma(X^s, Y^s; \omega) u(Y^s) dY^s, \tag{10}$$

with

$$K_\Gamma(X^s, Y^s; \omega) = w(Y^s)\delta(X^s - \phi^\omega(Y^s)), \tag{11}$$

where $X^s = (s, p_s)$ and $Y^s = (s', p_s')$ represent phase-space coordinates on the boundary. For X^s (and analogously for Y^s) this means that s parameterizes Γ and $p_s \in B_{|p|}^{d-1}$ denotes the momentum component tangential to Γ at s for fixed $H(X) = |p|^2$, where $B_{|p|}^{d-1}$ is an open ball in $\mathbb{R}^{d-1}$ of radius $|p|$. Hence $\partial\mathbb{P} = \Gamma \times B_{|p|}^{d-1}$ denotes the phase space on the boundary. Also, ϕ^ω is the invertible boundary map which takes a boundary phase space coordinate along its straight line trajectory (for homogeneous media) until it intersects the boundary again. Note that convexity is assumed to ensure ϕ^ω is well defined; non-convex regions can be handled by introducing a cut-off function in the shadow zone as in Ref. [15] or by subdividing the regions further.

The stationary density on the boundary induced by the initial boundary distribution $\rho_\Gamma^0(X^s, \omega)$ can then be obtained using

$$\rho_\Gamma(X^s, \omega) = \sum_{n=0}^\infty \mathcal{B}^n(\omega)\rho_\Gamma^0(X^s, \omega) = (I - \mathcal{B}(\omega))^{-1}\rho_\Gamma^0(X^s, \omega), \tag{12}$$

where $\mathcal{B}^n$ contains trajectories undergoing n reflections at the boundary. The resulting density distribution on the boundary $\rho_\Gamma(X^s, \omega)$ can then be mapped back into the interior region. One obtains the density (9) after projecting down onto coordinate space.

3.2. Discretization and basis representation

The long term dynamics are thus contained in the operator $(I - \mathcal{B})^{-1}$ and standard properties of Perron-Frobenius operators ensure that the sum over n in Eq. (12) converges for non-vanishing dissipation, or in open systems. In order to evaluate $(I - \mathcal{B})^{-1}$ a finite dimensional approximation of the operator $\mathcal{B}$ must be constructed. In Ref. [8,9] basis expansions have been applied in both position and momentum coordinates, which is straightforward to implement using univariate expansions in each argument for $\Omega \subset \mathbb{R}^2$. However, it is not straightforward to construct a general orthogonal basis with independent spatial arguments when $\Omega \subset \mathbb{R}^3$. For this reason we employ a boundary element triangulation of Γ, with a zero order basis approximation on each element for any L^2-orthonormal basis, which essentially results in a scaled piecewise constant boundary element approximation. This type of approximation is also often referred to as Ulam's method [23], although here such an approximation would be performed in full phase space, rather than just in its spatial component.

For the approximation in the momentum argument we choose a basis orthogonal in L^2 for consistency with the spatial approximation. We choose a Legendre polynomial basis for this purpose due to good convergence properties without requiring periodic boundary conditions [18]. Note that for $\Omega \subset \mathbb{R}^2$, then $p_s \in (-|p|, |p|)$, and for $\Omega \subset \mathbb{R}^3$ then in polar coordinates $p_s \in [0, |p|) \times [-\pi, \pi)$. Denote by $\tilde{p}_s$ a re-scaling of p_s to $(-1, 1)$ or $[-1, 1) \times [-1, 1)$ for the two and three-dimensional cases, respectively. Let us also denote

$$\widetilde{P}_\beta(p_s) = \frac{1}{\sqrt{|p|}} P_\beta(\tilde{p}_s), \tag{13}$$

for $\Omega \subset \mathbb{R}^2$, where P_β is the Legendre polynomial of order β. For $\Omega \subset \mathbb{R}^3$, $\beta = (\beta_1, \beta_2)$ is a multi-index of non-negative integers. Let us write $p_s = (p_k, p_\theta)$ and likewise $\tilde{p}_s = (\tilde{p}_k, \tilde{p}_\theta)$. Denote

$$\widetilde{P}_\beta(p_s) = \frac{2}{|p|\sqrt{\pi}} P_{\beta_1}(\tilde{p}_k) P_{\beta_2}(\tilde{p}_\theta). \tag{14}$$

Explicitly the overall approximation is then of the form

$$\rho_\Gamma(X^s,\omega) \approx \sum_{\alpha=1}^{n}\sum_{\beta=0}^{N} \rho_{(\alpha,\beta)} b_\alpha(s)\widetilde{P}_\beta(p_s), \tag{15}$$

where N is the order of the basis expansion, n is the number of elements and b_α denotes the scaled (for orthonormality in an L^2 inner product) piecewise constant boundary element basis function $b_\alpha(s) = 2^{(1-d)/2}/\sqrt{A_\alpha}$ for s in element α, and zero elsewhere. Here A_α is the surface area of element α in the three-dimensional case and the length of element α in the two dimensional case for $\alpha = 1,\ldots,n$. The coefficient vector $\rho_{(\alpha,\beta)}$ in (15) is labelled in terms of the multi-index (α,β). Note that in the three-dimensional case β is itself a multi-index and the sum over β in (15) is a double sum.

The matrix approximation B of $\mathcal{B}(\omega)$ for the case $\Omega \subset \mathbb{R}^2$ is computed in variational form using the basis approximations outlined above as follows

$$\begin{aligned} B_{(l,m),(\alpha,\beta)} &= \frac{2m+1}{4}\int_{\partial\mathbb{P}}\int_{\partial\mathbb{P}} \widetilde{P}_m(p_s) b_l(s) K_\Gamma(X^s,Y^s;\omega)\widetilde{P}_\beta(p'_s) b_\alpha(s') dY^s dX^s \\ &= \frac{2m+1}{4}\int_{\partial\mathbb{P}} w(Y^s)\widetilde{P}_m(\phi_p^\omega(Y^s)) b_l(\phi_s^\omega(Y^s))\widetilde{P}_\beta(p\prime_s) b_\alpha(s') dY^s, \end{aligned} \tag{16}$$

where K_Γ is the boundary operator kernel, Eq. (11). Here we write $\phi^\omega = (\phi_s^\omega, \phi_p^\omega)$, to denote the splitting of the position and momentum parts of the boundary map. Recall also that $X^s = (s,p_s)$ and $Y^s = (s',p'_s)$. The only changes for the three-dimensional case are that the indexing is slightly more complicated due to m and β becoming multi-indices and the definitions of $\widetilde{P}_\beta$ changes from Eq. (13) to Eq. (14). The prefactor changes from $(2m+1)/4$ to $(2m_1+1)(2m_2+1)/16$. Note that the additional division by 2 from the standard orthonormal inner product prefactor for Legendre polynomials comes from the fact that the spatial basis function is treated as a Legendre polynomial of order 0. Obtaining the boundary map ϕ^ω is not always straightforward, particularly for general three-dimensional geometries, and hence we write the operator in terms of trajectories with fixed start and end points, s' and s, as follows

$$B_{(l,m),(\alpha,\beta)} = \frac{2m+1}{4}\int_\Gamma\int_\Gamma w(Y^s)\widetilde{P}_m(p_s(s,s')) b_l(s)\widetilde{P}_\beta(p'_s(s,s')) b_\alpha(s')\left|\frac{\partial p'_s}{\partial s}\right| ds' ds. \tag{17}$$

The resulting boundary integral formulation containing a pair of integrals over boundary coordinates bears a resemblance to standard variational Galerkin boundary integral formulations such as in [24]. Note the momenta $p_s(s,s')$ and $p'_s(s,s')$ are now considered to be functions of the boundary position coordinates. In particular for the two-dimensional case $p_s(s,s') = |p|\hat{t}\cdot(r-r')/L$ and $p'_s(s,s') = |p'|\hat{t}'\cdot(r-r')/L$, where $\hat{t},\hat{t}'$ are unit tangent vectors to Γ at s,s', respectively. Also, L is the trajectory length from s' to s and r,r' are the cartesian coordinates corresponding to the parameter values s,s', respectively. In the three-dimensional case one can define momenta tangential to the boundary with respect to the local tangential coordinate system $(\hat{t}_1,\hat{t}_2)$ in any boundary element, that is, $p_{s1}(s,s') = |p|\hat{t}_1\cdot(r-r')/L$ and $p_{s2}(s,s') = |p|\hat{t}_2\cdot(r-r')/L$ (with $\hat{t}_1$ and $\hat{t}_2$, unit vectors as before). In order to obtain the momenta in the polar coordinate system $p_s = (p_k,p_\theta)$ used in (14) we define $p_k = \sqrt{p_{s1}^2+p_{s2}^2}$ and $p_\theta = \arctan(p_{s2}/p_{s1})$. Analogous definitions hold for $p'_s = (p'_k,p'_\theta)$.

Once the matrix B has been computed the values of $\rho_{(\alpha,\beta)}$ in (15) may be evaluated using Eq. (12) by solving

$$\underline{\rho} = (I-B)^{-1}\underline{\rho}^0, \tag{18}$$

where $\underline{\rho}$ has components $\rho_{(\alpha,\beta)}$ and

$$\rho^0_{(\alpha,\beta)} = \frac{2\beta+1}{4} < \rho^0_\Gamma(X^s,\omega), \quad \widetilde{P}_\beta(p_s) b_\alpha(s) >,$$

where $<\cdot,\cdot>$ is the standard L^2 inner product.

After solving Eq. (18) one has an approximation for the density distribution on the boundary ρ_Γ given by (15). This distribution is then mapped back into the interior region by projecting onto position space, that is for $\Omega_i \subset \mathbb{R}^2,\ i = 1,\ldots,N_\Omega$,

$$\rho(r,\omega) = \int \rho(r,p)dp, = \iint \rho^\Gamma(X^s,\omega)\delta(|p|^2-|k_i|^2)|p|d|p|d\Theta, \tag{19}$$

where $(|p|,\Theta)$ is a polar coordinate system for p, see [25] for details. The only difference in $\mathbb{R}^3$ is that one integrates over a sphere of radius $|p|$, rather than a circle.

3.3. Subsystems and links to SEA

Recall the splitting into subsystems $\Omega_i,\ i = 1,\ldots,N_\Omega$ introduced earlier. The dynamics in each subsystem are considered separately so that both variability in the wave velocity c_i and non-convex domains may be handled easily. Coupling between sub-elements can then be treated as losses in one subsystem and source terms in another. Typical subsystem interfaces are

surfaces of reflection/transmission due to sudden changes in material parameters or local boundary conditions. We describe the full dynamics in terms of subsystem boundary operators $\mathcal{B}_{ij}$; flow between Ω_j and Ω_i is only possible if subsystem i and j have a common boundary. One obtains $\mathcal{B}_{ij}$ by replacing K_Γ in the definition (10) with

$$K_{ij}(X_i^s, X_j^s) = w_{ij}(X_i^s)\delta\left(X_i^s - \phi_{ij}^\omega(X_j^s)\right), \tag{20}$$

where ϕ_{ij}^ω is the boundary map in subsystem j mapped onto the boundary of the adjacent subsystem i and X_i^s are the boundary coordinates of Ω_i. Note that the domain of integration in (10) now becomes $\partial\mathbb{P} = \partial\Omega_j \times B_{|p|}^{d-1}$, where $|p| = k_j$. The weight w_{ij} contains reflection and transmission coefficients characterizing the coupling at the interface between Ω_j and Ω_i. It also contains a damping factor of the form $\exp(-\mu_i L)$ where μ_i is the damping coefficient in Ω_i as before and L is the length of the trajectory from s' to s as before.

Repeating the steps in the previous subsection but instead using the operator above results in a basis function representation spanning all subsystems, see [8,9] for more details. Here we employ a boundary mesh ensuring that the boundary of an interface between two subsystems only intersects element boundaries and not their interiors. An SEA treatment emerges when approximating the individual operators $\mathcal{B}_{ij}$ in terms of constant functions only [8]. Here this corresponds to an approximation in terms of the lowest order basis functions in momentum space only, together with a coarse spatial mesh consisting of only one element per subsystem, or more typically a piecewise constant approximation on a mesh with continuity enforced within each subsystem. In this case the matrix B can be reduced to one element per subsystem. The matrix entry B_{ij} gives the mean transmission rate from subsystem j to subsystem i. It is thus equivalent to the coupling loss factor used in standard SEA equations [2]. The resulting full N_Ω-dimensional B matrix yields a set of SEA equations using the relation (12) after mapping the boundary densities back into the interior.

4. Numerical results

4.1. Verification in 2D for coupled two-cavity problems

In this section we consider two-dimensional polygonal domains whose boundaries are meshed by subdividing each side into equidistant sections governed by a mesh parameter Δx. The number of elements on any given side is computed using the integer part of the side length divided by Δx. The Jacobian from (17) is written in the form

$$\left|\frac{\partial p_s'}{\partial s}\right| = \frac{k_j(n\cdot(r-r'))(n'\cdot(r-r'))}{L}, \tag{21}$$

where n and n' are the internal unit normal vectors to Γ at r and r', respectively. In order to treat the corner singularities in (21), Gaussian quadrature is employed where end-points are not included as quadrature points. The convergence of the quadrature rules is still slow due to the peak in the integrand at corners. Telles' transformation techniques are employed to speed up the convergence [26].

A number of two-cavity systems are considered as shown in Fig. 1. Configuration A features irregular shaped, well separated pentagonal subsystems. In configuration B the size of the interface between the subsystems is increased reducing their dynamical separation. Configuration C includes a rectangular left-hand subsystem channelling rays out of the subsystem and introducing long-range correlations in the dynamics. In addition, the source is further from the intersection of the two subsystems. Note that SEA results are in general insensitive to the position of the source, whereas actual trajectory calculations may well depend on the exact position.

In [8,9] it is demonstrated, as expected, that SEA works well for configuration A, but not so well for configurations B and C. In this communication we seek to verify our new approach against results from previous work. In particular we discuss the relative computational efficiency of the new and old approaches and how they scale as the level of precision in the model is increased. Energy distributions have been studied as a function of the frequency with a hysteretic damping factor $\eta = 0.01$, where $\mu_i = \omega\eta/(2c_i)$ for $i = 1, 2$. Here and in the remainder of this section the subsystems are numbered 1,2 from left to

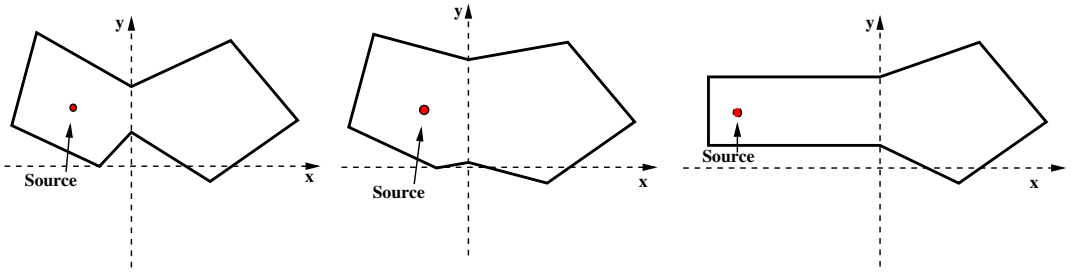

Fig. 1. Coupled two-domain systems: configurations A, B and C respectively.

right. The other parameters are set to unity for simplicity, that is $\varrho_i = c_i = 1$ for $i = 1, 2$. For this reason the subsystem interface reflection and transmission coefficients appearing in the weight term in (20) are simply 0 and 1, respectively.

Fig. 2 shows the the boundary element DEA results for configurations A, B and C together with solutions of the wave Eq. (1) with Dirichlet boundary conditions obtained using a discontinuous Galerkin finite element method; for details of the method, see [9]. Explicitly we compute the energy ratios between the two subsystems $R = ||G_1||^2/||G_2||^2$ where

$$||G_i||^2 := \int_{\Omega_i} |G(r, r_0; \omega)|^2 dr, \quad i = 1, 2. \tag{22}$$

The dotted lines each represent a simulation at a different frequency in the range ± 5 Hz of the frequencies used for the boundary element DEA calculations. In all three cases good convergence of the method is demonstrated. For configuration B, shown in the central subplot, the results converge with a slightly lower order of approximation. This may be due to the irregular geometry and the wide opening linking the subsystems meaning that the energy is very evenly distributed throughout the whole domain. Hence lower order spatial approximations will be reasonably good. Note that the results do not necessarily improve with increasing frequency, since the damping is frequency dependent. For configuration C this actually means that relatively high order computations are required to capture the rapid decay of the solution along the rectangular channel; similar observations were also made in [9].

Table 1 shows the total computational times for the 10 Hz calculation in Fig. 2 using both boundary element DEA and comparing with a previous approach where a Chebyshev basis is employed in full phase space [9]. That is to say n has no meaning for the Chebyshev case and N is the order of Chebyshev basis approximation in both the position and momentum arguments. The computations were performed using a desktop PC with a 2.83 GHz dual core processor, although the code was not parallelized. The total computational expense is considerably reduced using the current boundary element DEA approach. In addition the computational cost of boundary element DEA is growing more slowly as the precision of the model is increased. This will be very important for the three-dimensional case where the number of degrees of freedom in the model

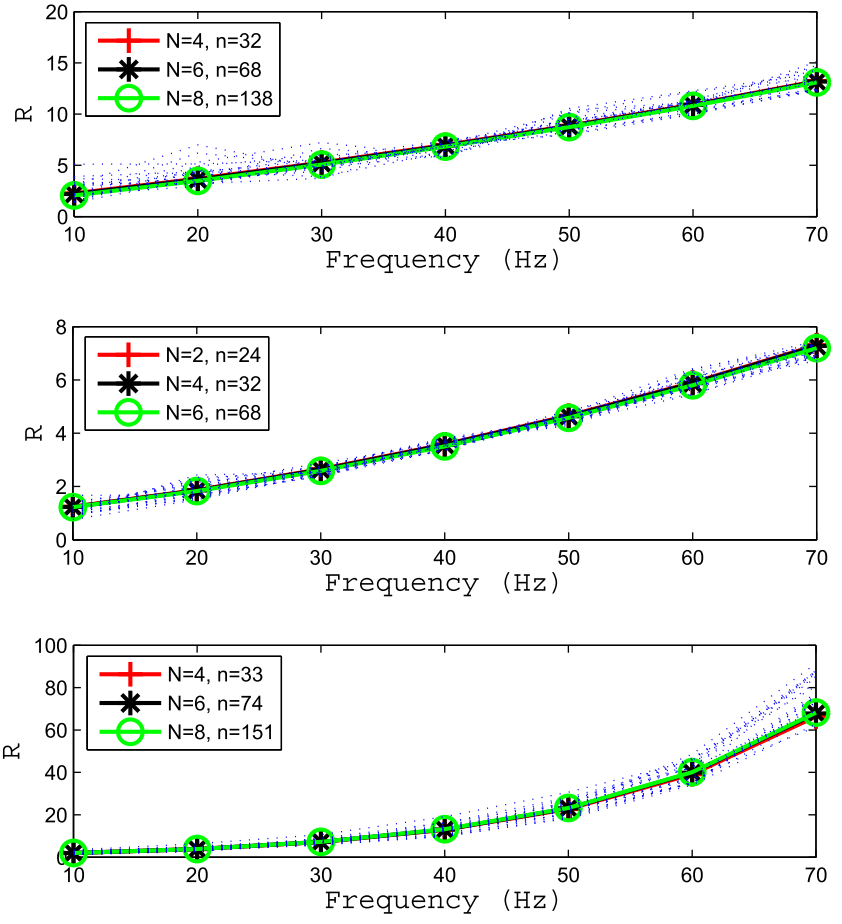

Fig. 2. Ratio of total energies $R = ||G_1||^2/||G_2||^2$ in configurations A, B and C respectively. The dotted lines correspond to FEM calculations of the full wave problem.

Table 1
Computational times for Configuration A with $f = 10$Hz

n	N	Total computational times (s):	
		Boundary element	Chebyshev
32	4	140	590
68	6	280	3910
138	8	850	31,290

will increase more quickly. The main reason for the time saving stems from the fact that in the boundary element approach the integrals in the definition of the transfer matrix B (16) are computed in smaller regions and the approximation functions in the integrands are generally simpler. As such these integrals may be evaluated using far fewer quadrature points than in the Chebyshev approach. When we consider that the Chebyshev algorithm was already a considerable saving on the original DEA methods discussed in [8] one can see how far we have come. Since the parameters for configurations B and C are similar to those for configuration A, the computational times are roughly the same for the same orders of approximation.

4.2. Applications in 3D

In this section we consider some three-dimensional domains whose boundaries have been triangulated using the Tetgen freeware automated mesh generating package ("http: tetgen.berlios.de"). The Jacobian from (17) may be computed using standard formulae for global, local and polar coordinate transformations along with several applications of the chain rule. As before the Jacobian introduces singularities in the integrals along edges and at vertices of the domain. Again Gaussian quadrature and a carefully chosen application of Telles' transformation techniques are employed to ensure fast convergence of the numerical integration procedures.

The first example we consider is that of a cuboid $(x, y, z) \in (-1, 1) \times (-0.5, 0.5) \times (-0.5, 0.5)$ with Dirichlet boundary conditions (all distances are given in meters). The source point is taken as $(-0.9, 0.1, 0.1)$ and the same frequency and damping correspondence is used as in the two-dimensional examples with $\varrho = c = 1$ (with units kg/m^3 and m/s, respectively). Fig. 3 shows the computed energy distributions inside the cuboid along the x-axis. The method is compared against discontinuous Galerkin finite element method (FEM) computations, which are averaged over 17 frequencies within ± 2 Hz of the (central) frequency used for the boundary element DEA computation. Further details of the FEM techniques employed here can be found in [9] and references therein. The reverberation time T_{60} for this cavity may be computed as a function of the damping level, at 10 Hz we have approximately $cT_{60} = 112.9$ m. At 20 Hz the corresponding figure is $cT_{60} = 56.4$ m. Using standard formulae from, for example [27], one may now evaluate the corresponding Schröder frequencies and critical distances. The modal densities may be computed as approximately 2529 Hz^{-1} at 10 Hz and 10085 Hz^{-1} at 20 Hz which leads to estimates of the modal overlap factor [27] of approximately 50 and 390, respectively. We are thus well into the regime where SEA is usually considered valid.

The dashed line in Fig. 3 shows an approximation with a coarse mesh and where the energy density is assumed constant over all possible directions of rays approaching the boundary from the interior. The computation time for such an

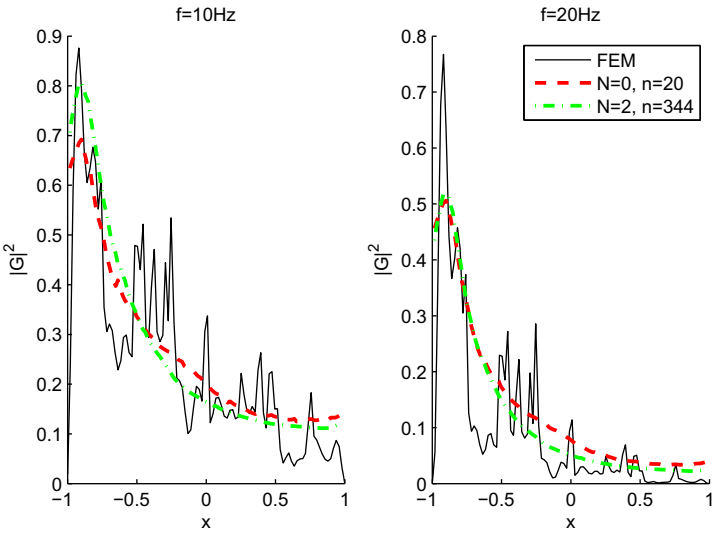

Fig. 3. Energy distribution along the x-axis in the cuboid example.

approximation is typically a few seconds per frequency. The dash-dot line shows a higher order approximation where we have refined the mesh until the solution appears reasonably converged by eye, in this case 344 elements were employed. Also due to the relatively low dissipation levels in these plots a low order approximation in momentum (quadratic) was sufficient to give reasonably converged results. The computation time for this plot was approximately 16 h, and this cost is heavily dominated by the time taken to set up the linear system. Solving the linear system directly and post-processing the data forms only a very minor part of the total computational expense. The cost of the setup procedure scales approximately as $O(n^2(N+1)^4)$, although quadrature costs can distort this. Increasing N generally increases the quadrature costs, whereas increasing n reduces them. The rapid increase in expense as N is increased can be offset by the fact that in general we expect a relatively low value of N to be sufficient [8], and that the degrees of freedom introduced by increasing N can be computed independently and thus are extremely suitable for parallelisation.

It has been demonstrated that in the low damping regime SEA can provide good approximations even in regular structures [9], which explains why the coarse approximation here is still reasonably good. However, one notices an improvement in the match with the FEM data at both the peak and tail of the plot for both frequencies considered when the higher order approximation method is employed. There is, however, a significant computational cost associated with this increased precision.

As a second example, we consider an open car cavity as discussed in [28] and shown in Fig. 4. The source point is located on the base of the cavity at $(0.6, 0.0, 0.4)$, with distances in meters as before. Here we consider Dirichlet boundary conditions except along the roof, which is assumed to be non-reflecting along the subsection shown in black in Fig. 4, between x = 1.0 m and x = 1.8 m. Physically this corresponds to an opening in the cavity with identical media in both the interior and exterior. The reverberation time T_{60} for this cavity may be evaluated using Sabine's formula, see for example [10], and we obtain $cT_{60} = 265.3$ m showing that the car cavity is more reverberant than the cuboid example. Here the DEA computation is frequency independent, but to leading order we have the correspondence $f \approx \sqrt{1.47Mc^3}$, where M is the modal overlap factor, so one can judge a valid frequency range for the plot from this data. For example with $c = 340\ \mathrm{ms}^{-1}$ and if we require $M > 1$, then $f > 7601$ Hz.

Fig. 5 shows the amplitude $|G|$ plotted in the interior of the cavity along the midplane $z = 0.85$ m. The jagged diagonal edge shown in Fig. 5 is merely an artifact of the plotting and interpolation of the amplitude at discrete points, and is actually smooth in the model as shown in Fig. 4. In three dimensions the amplitude of Green's function for the Helmholtz equation is independent of frequency, and thus the only frequency dependence in the cuboid example was due to the damping being frequency dependent. No damping is incorporated in this example and energy losses only occur through the open roof, meaning that the plots here are now frequency and wavenumber independent. The three subplots show successively higher order approximations from upper to lower and convergence in the plots is evident due to the increased similarity between the lower two plots. Directivity in the wave field plays a much stronger role in this example due to the localised dissipation at the opening of the cavity. For this reason it was necessary to employ a higher order momentum basis approximation than in the previous example; the plot is reasonably converged choosing $N = 4$. The computational times were a few seconds for the upper subplot, eleven hours for the central subplot and three days for the lower plot. The scaling of the computing time mirrors the $(N+1)^4$ scaling of the matrix dimensions. The computational overhead thus becomes significant if higher order momentum basis functions become necessary making the method slow at present; our 3D study thus gives a proof-of-principle, but further improvements need to be found to yield a competitive 3D method.

The upper plot in Fig. 5 has a markedly different appearance to the other subplots showing that the most coarse approximation is not good in this case. One reason for this is the much stronger directivity of the wave field compared with the

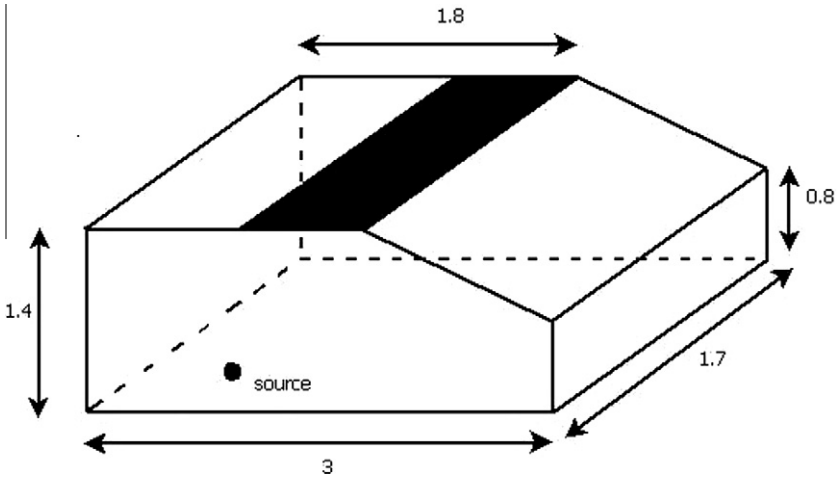

Fig. 4. The car cavity showing the source point and the open roof (black) acting as absorbing boundary.

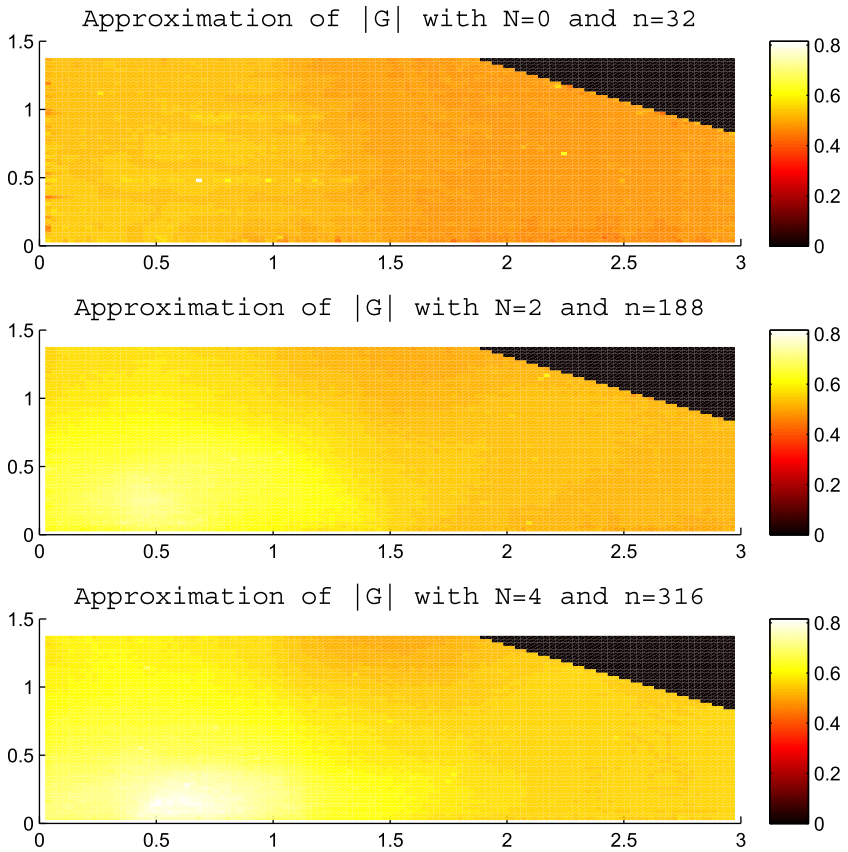

Fig. 5. Amplitude $|G|$ along the plane z = 0.85 for the car cavity example.

previous example. One can clearly see how in the upper plot the solution is more slowly varying and distributed more uniformly as you move away from the source point. In the lower plot one sees a noticeable dip in the amplitude close to the non-reflecting boundary. Also the increased intensity around the source point stretches more in the horizontal direction than the vertical direction in the lower plot, but is more evenly distributed in the other plots. In all three subplots the wave amplitude is greater in the region to the left of the opening (for $x < 1$ m) since in this region there are many possible ray trajectories that remain trapped in the cavity for a long time before exiting through the opening. This is also true for the region $y < 0.8$ m and hence the greatest intensities are observed in the intersection of these two regions. In billiard dynamics these trajectories are known as near-bouncing-ball orbits, see for example [29].

5. Conclusions

A new approach to determining the distribution of mechanical and acoustic wave energy in complex built up structures has been discussed. The methodology has been carefully chosen to permit application to two or three dimensional problems. Using boundary element meshes for three dimensional problems renders the method applicable to general domains and removes the need to determine an orthogonal spatial basis for each geometrically different example. The application of the method to some well studied two-dimensional examples has shown it to be efficient and scale favourably as the number of degrees of freedom in the model is increased compared with previous DEA approaches. Examples in three dimensions were also considered showing both the applicability and versatility of the method, but also its high computational cost as the number of degrees of freedom is increased. We have also seen however that in some cases a low order and fast computation yields reasonably good results. The suitability of the method for parallel processing means that with greater computing resources it has the potential to be employed in larger and more complicated configurations than those considered here.

Acknowledgements

Support from the EPSRC(Grant EP/F069391/1) and the EU(FP7IAPP Grant MIDEA) is gratefully acknowledged. The authors also wish to thank inuTech Gmbh, Nürnberg for Diffpack guidance and licences and Hanya Ben Hamdin and Dmitrii Maksimov for helpful discussions.

References

[1] R.H. Lyon, Statistical analysis of power injection and response in structures and rooms, J. Acoust. Soc. Am. 45 (1969) 545–565.
[2] R.H. Lyon, R.G. DeJong, Theory and Application of Statistical Energy Analysis, second ed., Butterworth, Heinemann, Boston, MA, 1995.
[3] R.J.M. Craik, Sound Transmission through Buildings using Statistical Energy Analysis, Gower, Hampshire, UK, 1996 (p. 261).
[4] A.S. Glasser, An Introduction to Ray Tracing, Academic Press, London, 1989.
[5] H. Kuttruff, Room Acoustics, fourth ed., Spon, London, 2000.
[6] V. Cerveny, Seismic Ray Theory, Cambridge University Press, Cambridge, UK, 2001.
[7] S. Kulkarni, F.G. Leppington, E.G. Broadbent, Vibrations in several interconnected regions: a comparison of SEA ray theory and numerical results, Wave Motion 33 (2001) 79–96.
[8] G. Tanner, Dynamical energy analysis-determining wave energy distributions in vibro-acoustical structures in the high-frequency regime, J. Sound Vib. 320 (2009) 1023–1038.
[9] D.J. Chappell, S. Giani, G. Tanner, Dynamical energy analysis for built-up acoustic systems at high frequencies, J. Acoust. Soc. Am. 130 (3) (2011) 1420–1429.
[10] G. Tanner, N. Søndergaard, Wave chaos in acoustics and elasticity, J. Phys. A 40 (2007) R443–R509.
[11] K.H. Heron, Advanced statistical energy analysis, Phil. Trans. Roy. Soc. Lond. A 346 (1994) 501–510.
[12] R.S. Langley, A wave intensity technique for the analysis of high frequency vibrations, J. Sound Vib. 159 (1992) 483–502.
[13] R.S. Langley, A.N. Bercin, Wave intensity analysis for high frequency vibrations, Phil. Trans. Roy. Soc. Lond. A 346 (1994) 489–499.
[14] A. Le Bot, A vibroacoustic model for high frequency analysis, J. Sound Vib. 211 (1998) 537–554.
[15] A. Le Bot, Energy transfer for high frequencies in built-up structures, J. Sound Vib. 250 (2002) 247–275.
[16] A. Le Bot, Energy exchange in uncorrelated ray fields of vibroacoustics, J. Acoust. Soc. Am. 120 (3) (2006) 1194–1208.
[17] R.T. Farouki, T.N.T. Goodman, T. Sauer, Construction of orthogonal bases for polynomials in Bernstein form on triangular and simplex domains, Comput. Aided Geom. Design 20 (2003) 209–230.
[18] J.P. Boyd, Chebyshev and Fourier Spectral Methods, 2nd ed., Dover Mineola, NY, 2000.
[19] O. Runborg, Mathematical models and numerical methods for high frequency waves, Commun. Comput. Phys. 2 (5) (2007) 827–880.
[20] P. Cvitanović, R. Artuso, R. Mainieri, G. Tanner, G. Vattay, Chaos: Classical and Quantum, Niels Bohr Institut, Copenhagen, ChaosBook.org, 2009.
[21] M.C. Gutzwiller, Chaos in Classical and Quantum Mechanics, Springer, New York, 1990. Chapter 17..
[22] M.A. Sepulveda, S. Tomsovic, E.J. Heller, Semiclassical propagation: how long can it last?, Phys Rev. Lett. 69 (3) (1992) 402–405.
[23] J. Ding, A. Zhou, Finite approximations of Frobenius–Perron operators. a solution of Ulam's conjecture to multi-dimensional transformations, Physica D 92 (1996) 61–68.
[24] G. Schmindlin, Ch. Lage, Ch. Schwab, Rapid solution of first kind boundary integral equations in $\mathbb{R}^3$, Eng. Anal. Bound. Elem. 27 (2003) 469–490.
[25] D.J. Chappell, G. Tanner, Solving the stationary Liouville Equation via a Boundary Element Method, J. Comput. Phys., in press.
[26] J.C.F. Telles, A self-adaptive co-ordinate transformation for efficient numerical evaluation of general boundary element integrals, Int. J. Numer. Meth. Eng. 24 (1987) 959–973.
[27] C.H. Hansen, Noise Control: From Concept to Application, Taylor & Francis, Abingdon, 2005.
[28] J. Rejlek, H. Priebsch, Wave based technique for the analysis of fully coupled structural-acoustic unbounded problems, Proceedings of ISMA, Leuven, 2010.
[29] G. Tanner, How chaotic is the stadium billiard? a semiclassical analysis, J. Phys. A 30 (1997) 2863–2888.